Soft Matter

Accepted Manuscript

ROYAL SOCIETY OF CHEMISTRY

www.rsc.org/softmatter

ARTICLE TYPE www. rsc.org/xxxxxx | XXXXXXXX

The spatial-temporal characteristics of type I collagen-based extracellular matrix†

Christopher Jones,[a] **Long Liang,**[b] **Daniel Lin,** [a] **Yang Jiao,** [c*] **and Bo Sun,** [d*]

Received Xth XXXXXXXXXX 20XX, Accepted Xth XXXXXXXXX 20XX
First published on the web Xth XXXXXXXXXX 200X
DOI: 10.1039/b000000x

Type I collagen abounds in mammalian extracellular matrix (ECM) and is crucial to many biophysical processes. While previous studies have mostly focused on bulk averaged properties, here we provide a comprehensive and quantitative spatial-temporal characterization of the microstructure of type I collagen-based ECM as the gelation temperature varies. The structural characteristics including the density and nematic correlation functions are obtained by analyzing confocal images of collagen gels prepared at a wide range of gelation temperatures (from 16 ^{o}C to 36 ^{o}C). As temperature increases, the gel microstructure varies from a "bundled" network with strong orientational correlation between the fibers to an isotropic homogeneous network with no significant orientational correlation, as manifested by the decaying of length scales in the correlation functions. We develop a kinetic Monte-Carlo collagen growth model to better understand how ECM microstructure depends on various environmental or kinetic factors. We show that the nucleation rate, growth rate, and an effective hydrodynamic alignment of collagen fibers fully determines the spatiotemporal fluctuations of the density and orientational order of collagen gel microstructure. Also the temperature dependence of the growth rate and nucleation rate follow the prediction of classical nucleation theory.

INTRODUCTION

As a major component of mammalian extracellular matrix (ECM) such as in skin, tendon, and organs, type I collagen (collagen I) makes up about 25% of the whole-body protein content[1]. Physiologically, collagen I molecules are synthesized by stromal cells, such as fibroblasts, in order to maintain the integrity of the extracellular matrix. When such functions are compromised, the human body develops several diseases, such as Ehlers-Danlos syndrome and Infantile cortical hyperostosis[2].

Collagen I has been widely used in tissue engineering as a scaffold protein[3,4] because it naturally forms a gel of hierarchical structure that is compatible for mammalian cell cultures and hosting a variety of growth factors[5]. Monomeric collagen I can self-assemble into fibrils that are approximately 300 nm long and 1.5 nm in diameter. The fibrils further bundle together to form thick fibers that are more than 1 μm long and 100 nm in diameter. These fibers dominate the mechanical and transport properties of collagen I gel[6,7] and they can be directly visualized without tagging probes using phase contrast[8,9], confocal reflection[10–12] , or second harmonic generation microscopy[13,14].

The fiber networks of collagen gel natively support the adhesion of many types of cells. As a result, it has been adapted as a popular model ECM for 2D and and 3D cell culture. Many studies have shown that cells are sensitive to the fiber structure of collagen ECM. For instance, dense and rigid fibers promote growth of cancer cells[15,16]. Highly-aligned collagen fibers may induce malignant transition of mammary acini into invasive phenotypes[17]. The microstructure heterogeneity of collagen gel have also been shown to guide the cell migration through durotaxis[18] and contact alignment[19]. In addition, the physical properties of collagen ECM such as the effective diffusion coefficient[7,20–29] and stress distribution[6,30–35], which are respectively crucial to the chemical and mechanical signaling between the cells, are determined by the fiber network configurations. These observations highlight the diverse physical cues supported by collagen ECM, and the importance to understand the factors that determine the microstructures of a collagen gel.

To date, most structural characterization of collagen gel, such as porosity[36,37], pore-size distribution[6,7,38–40], and turbidity[10,41], has mainly focused on the bulk averaged properties. There is lack of data to characterize the spatial heterogeneity of the fiber network[42], and how the matrix microstructure can be tuned. In this article, by employing sophisticated statistical morphological descriptors devised in condensed

† Electronic Supplementary Information (ESI) available: [details of any supplementary information available should be included here]. See DOI: 10.1039/b000000x/

[a] *Department of Physics, Oregon State University, Corvallis, OR, 97331*
[b] *Department of Physics, Arizona State University, Tempe, AZ, 85287*
[c] *Materials Science and Engineering, Arizona State University, Tempe, AZ 85287, Telephone: 480-965-4560, Email: yang.jiao.2@asu.edu*
[d] *Department of Physics, Oregon State University, Corvallis, OR, 97331, Telephone: 541-737-8203, Email: sunb@onid.orst.edu*

matter physics[43] and heterogeneous material theory[44–46], we provide a comprehensive and quantitative spatial-temporal characterization of the microstructure of type I collagen-based ECM as the gelation temperature varies. In particular, we combine confocal microscopy and image correlation analysis to systematically study the fibrous configurations of collagen gel. We characterize the growth kinetics as well as the static microstructure of collagen gel by quantifying the spatial fluctuations in fiber density and orientation with the density and nematic correlation functions, respectively.

In order to better understand how collagen ECM microstructure depends on the environmental and kinetic factors, we have developed a kinetic Monte-Carlo model based on the experimental measurements to simulate the growth dynamics of a collagen gel at fixed gelation temperatures. Our model suggests that the static structure of collagen gel is inherently connected with the growth kinetics. In particular, it shows that the nucleation rate, growth rate, and an effective hydrodynamic alignment of collagen fibers fully determines the spatiotemoral fluctuations of the density and orientational properties of collagen gel microstructure. Our model also enables us to determine the temperature dependence of the nucleation rate and growth rate, which are difficult to directly measure in experiments.

RESULTS

GROWTH DYNAMICS OF COLLAGEN MATRIX

In order to quantify the structural evolution of collagen fiber network during gelation, we used reflection mode of laser scanning confocal microscope (LSCM, Leica SPE) to image a 2D slice of a thick collagen gel. Fig. 1 demonstrates the microstructural dynamics in a typical gelation process. The self-assembly of collagen matrix initiated immediately from time zero, when 2 mg/mL type I collagen in acetic acid was neutralized by NaOH and buffered by 10 × PBS (phosphate buffered saline) at room temperature. At around 5 minutes, a few isolated fibers started to appear at random locations and moved diffusively. These initial fibers anchored the nucleation of more fibers to form clusters each consisting of a few distinguishable fibers. As gelation proceeded, the viscosity and the level of fiber entanglement increased. Finally, the fiber clusters were arrested and became the quenched structural heterogeneity after the gel was fully formed (Fig. 1 A, also see Supporting Material section S2). Using template-matching methods, we have also calculated the corresponding nematic field at different stages of gelation as shown in Fig. 1 B.

To characterize the spatial organization of the self-assembled fiber structure, we measure the two-point correlation of image intensity to approximate the density spatial fluctuation of the gel matrix :

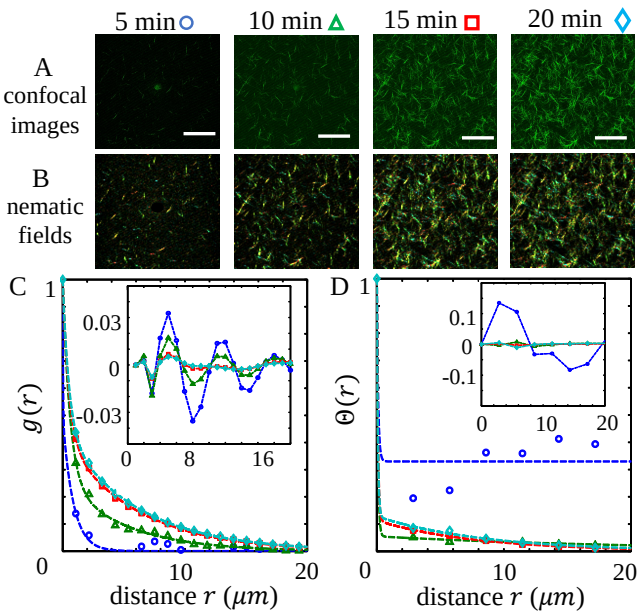

Fig. 1 The correlation analysis reveals the typical growth dynamics of type I collagen gel. Time zero corresponds to the moment when 2 mg/mL collagen solution was neutralized and maintained in 23 °C. A: time-lapse confocal reflection images taken at 5, 10, 15 and 20 minutes. B: The corresponding nematic field obtained by template matching method. The nematic field $\mathbf{s}$ is color coded in the HSV space: the hue channel is proportional to the complex angle of $\mathbf{s}$ and the value channel is proportional to the magnitude $|\mathbf{s}|$. C: The two-point intensity correlation function $g(r)$, dashed lines represent double exponential fittings. Inset: the residual of fitting $g(r)$ with double exponential function. D: The two-point nematic order correlation function, dashed lines represent double exponential fittings. Inset: the residuals of double exponential fitting.

$$g(r) = \frac{1}{\sigma^2} < \tilde{I}(\mathbf{r_0})\tilde{I}(\mathbf{r_0}+\mathbf{r}) >_{\mathbf{r}_0}$$
$$\tilde{I} = I - < I >, \text{ and } \sigma^2 = < \tilde{I}^2 > \quad (1)$$

Where $I(\mathbf{r_0})$ is the 8-bit gray scale image intensity and $\tilde{I}$ is the image offset by its global average. $g(r)$ characterizes how likely two points of distance r apart have the same content (background or collagen fiber, Fig. 1 C). The decay of $g(r)$ slows down at later time, and plateaus at around 20 minutes, consistent with the growth dynamics of the fiber clusters. $g(r)$ follows a double exponential function as $a_1 \exp(-l_1 r) + a_2 \exp(-l_2 r)$ with root mean square deviation (RMSD) less than 0.02 in all our data sets (Fig. 1 C inset). The two length scales l_1 and l_2 are well separated, typically differ by an order of magnitude, and are related with the fiber thickness and sizes of the fiber clusters, respectively (See Supporting Material section S3). In the beginning, when only a few fibers exist,

the dominant density spatial fluctuation is the fiber thickness l_1, hence $a_1 >> a_2$. At later time, the two weight coefficients become closer, and the heterogeneous density fluctuation of the self-assembled collagen fiber matrix can be characterized by the length scales l_1, l_2, which we will examine systematically at different gelation conditions.

In addition to the density heterogeneity of the collagen matrix discussed above, fiber orientations are characterized by 2-D nematic field $\mathbf{s}(\mathbf{r}) = \sum_n e^{2i\theta_n(\mathbf{r})}$ (Fig. 1B), where $\theta_n(\mathbf{r})$ is the angle between a fiber at position $\mathbf{r}$ with respect to an arbitrary direction (which we choose to be the horizontal axis of the image), and the extra factor 2 makes the nematic field invariant under reflection.

To obtain the nematic field from confocal images, we have developed a template-matching algorithm (see material and methods), which converts each confocal image (1024 X 1024 pixel resolution) into a 128 X 128 coarse-gained nematic field. The spatial organization of the fiber orientations can be evaluated by the two point correlation function of $\mathbf{s}$ defined as

$$\Theta(r) = |\frac{1}{<|\mathbf{s}|^2>} < \mathbf{s}(\mathbf{r_0})\mathbf{s}^*(\mathbf{r_0}+\mathbf{r}) >_{\mathbf{r}_0} | \qquad (2)$$

where $\Theta(r)$ characterizes how likely two points of distance r apart have the same orientation. Notice that only points with $|s| > 0$ contribute to the correlation function. Because $\mathbf{s}(\mathbf{r})$ is intrinsically coarse-gained, $\Theta(r)$ does not depend on the fiber thickness. Instead, it measures the directional persistence along a fiber and co-alignment between nearby fibers. As the gel is forming, $\Theta(r)$ decays slower at later times, because fibers elongate and form aligned "bundles", or clusters (Fig. 1D). $\Theta(r)$ can also be approximated with a double exponential function, although the geometric meaning is less obvious due to the coarse-gaining.

TEMPERATURE DEPENDENCE OF COLLAGEN MATRIX

After introducing the correlation functions to quantify the spatial fluctuation of density and nematic orders, we now study collagen gel formed at different environment temperatures T at a fixed concentration of 2 mg/mL. We made multiple gel samples for each temperature in glass bottom microwells. For each sample, we took a confocal z-stack starting from 10 μm above the glass bottom to avoid reflection of the glass and the z-step was set to equal the axial width of the point spread function (1.7 μm). In total for each gelation temperature we collected about 400 images in order to statistically characterize the microstructure of collagen gel.

Fig. 2 demonstrates the density spatial fluctuations using the 2-point correlation function $g(r)$. In Fig. 2A, $g(r)$ curves for different temperatures are grouped by colors (blue-green-red in the order of increasing temperature) and data point markers (circle-triangle-square-diamond in the order of increasing temperature). As temperature increases, $g(r)$ decays faster, which is consistent with smaller pore sizes (see Supporting Material section S4). Notice that the density spatial fluctuation does not have any systematic dependence with respect to the position of focal plane, or the distance between the glass bottom and image plane, suggesting a weak boundary effect when forming the gel (Fig. 2A, inset).

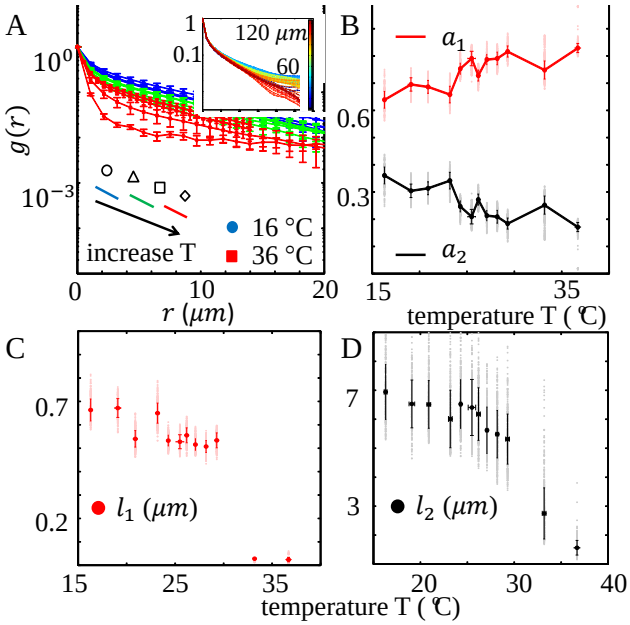

Fig. 2 The temperature dependence of the collagen gel microstructure revealed by density correlation function $g(r)$. A: (Log scale) Mean and standard deviation of $g(r)$ for gel formed at different temperatures and fixed concentration (2mg/mL). Each data point is calculated by sampling $\sim$ 400 images from multiple gel samples made in the same condition. Legend: blue circle, triangle, square, diamond represent 16, 19, 21, 23 °C; green circle, triangle, square, diamond represent 24, 25, 26, 27, °C; red circle, triangle, square, diamond represent 28, 29, 33, 36 °C. Inset: $g(r)$ for a typical gel sampled at different depth and plotted in the same scale of A. We take 2D slices of each gel from 10 μm to 130 μm away from the glass bottom in 1.7 μm steps (step size equals to the width of point spread function). Results for a typical sample are color coded by their relative distance from the glass bottom. B-D: The double exponential fitting parameters a_1, a_2, l_1, l_2 for each image (dotted scattering plot), and their means and standard deviations (solid lines and error bars).

Fig. 2B-C demonstrate the temperature dependence of the parameters a_1, a_2, l_1, and l_2 from double exponential fittings. As temperature grows, there are denser but shorter fibers, thus the weight $a_1 = 1 - a_2$ increases. l_1 slowly decreases just above the diffraction limit ($\approx$ 0.4 μm) until when gelation temperature T is greater than 30 °C, therefore the faster decay

of $g(r)$ at higher temperature is mainly due to the decrease of l_2. When T >30 °C, however, reduced fiber thickness (below the diffraction limit,[10]) and length, together with the increased gel turbidity lowered the image signal to noise ratio and greatly suppress the length scale l_1. In addition, we also find the length scale l_2 becomes less sensitive to temperature when T < 21 °C. As we will discuss below, this can be explained if the energy barrier for fiber growth is comparable to the thermal energy at $T \sim 21$ °C.

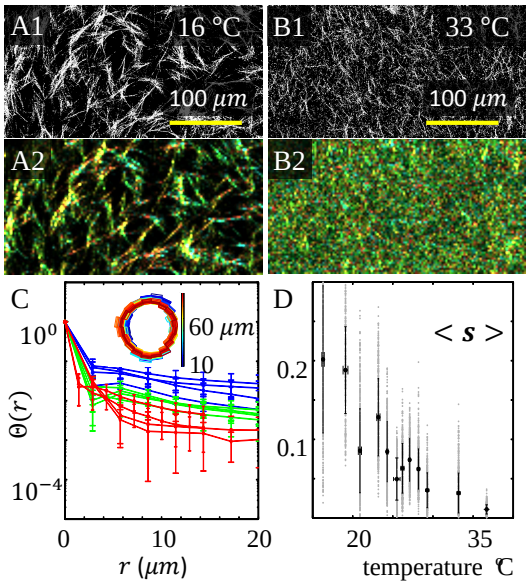

Fig. 3 The temperature dependence of the collagen gel microstructure revealed by nematic correlation $\Theta(r)$. A1: A typical confocal image of collagen gel formed at 16 °C, converted to binary to enhance the contrast. A2: The corresponding nematic field of the image in A1. The nematic field $\mathbf{s}$ is color coded in the HSV space: the hue is proportional to the complex angle of $\mathbf{s}$ and the value is proportional to the magnitude $|\mathbf{s}|$. B1-B2: A typical confocal image and the associated nematic field of gel formed at 33 °C. C: (Log scale) Mean and standard deviation of $\Theta(r)$ for gel formed at different temperatures and fixed concentration (2mg/mL). Each data point is calculated by sampling $\sim$ 400 images from multiple gel samples made in the same condition. Legend: same as in Fig. 2A. Inset: The angle distributions of a typical gel sampled at different focal depth (10 μm to 130 μm from the glass bottom in 1.7 μm steps). The histograms of the complex angles of $\mathbf{s}(\mathbf{r})$ for each slice are plotted in polar coordinate and are color coded by their relative distance from the glass bottom. D: The magnitude of global nematic order parameter $< \mathbf{s} >$ as a function of temperature. Data presented here are the results from individual images (dotted scattering plot), their means and standard deviations (solid lines and error bars).

The systematic change of collagen gel microstructure with respect to temperature is also evident from the nematic orders. As shown in Fig. 3A-B, at higher temperature, collagen fibers are shorter and more randomly oriented. As a result, the correlation in nematic field becomes shorter ranged (Fig. 3C). Similar to the density correlations, the nematic fields do not systematically depend on the depth of focal plane (Fig. 3C, inset), therefore we consider images taken at different depth as statistically independent.

When orientation of collagen fibers fluctuate strongly in space, we expect a small global nematic order $< \mathbf{s} >= \frac{1}{N}\sum_i \mathbf{s}(\mathbf{r}_i)$, where the average is taken over all subregions that contains a fiber. This is evident in Fig. 3D, where the global nematic order decreases monotonically as a function of T. The result suggests that at fixed chemical composition and collagen concentration, the gel microstructure depends on the gelation temperature in a manner that resembles ferromagnetic phase transition. Indeed, as T increases, the order parameter $< s >$ decreases and approaches zero continuously.

The above experimental measurements suggest that the self-assembly of collagen matrix is temperature sensitive. As the gelation temperature increases, the static microstructure of collagen gel evolves from clusters of long, aligned fibers to homogeneously distributed, short, and random oriented fibers. Interestingly, the same trend has been observed in connective tissues that are compromised by fibrosis[47]. To better understand the underlying physics that determines the self-assembled collagen ECM microstructures, we have developed a computational model to link the equilibrium gel configurations with the growth dynamics.

Kinetic Monte-Carlo Collagen Growth Model

To complement our experimental study of the effects of gelation temperature on the microstructure of the collagen network, we develop a kinetic Monte-Carlo method to simulate the gelation process. The goal of the kinetic MC method is not to simulate the full molecular details of each collagen fiber during the gelation process, but rather to understand, on a coarser scale, the effects of a number of controlling factors (e.g., gelation temperature) on final structure of the collagen network. Specifically, we model each fiber as a spheroclyinder, which is initially short and can grow in length due to polymerization at both ends. Two fibers can form a cross-link (corresponding to fiber entanglement in the collagen gel) if they are sufficiently close to one another. We consider the cross-linked fibers as a cluster. Individual fibers and clusters of fibers can diffuse in the solution. The associated effective diffusion coefficients depend on the size of the fiber/cluster as well as the viscosity of the solution, which increases dramatically as the gelation proceeds[12]. We note the detailed physical interactions between the collagen monomers and the resulting complex kinetics of the association and disassociation processes are not incorporated, as did in many first-principle and molecular dynamics models for biopolymer network self-assembly and dynamics[48–61]. However, we emphasize that our

meso-scale model is sufficient to reproduce the growth kinetics of the collagen gel, as we will show in the next section.

Two key parameters in our model are the nucleation rate n and fiber growth rate γ, both of which depend on the collagen concentration c and gelation temperature T. In particular, we consider that n and γ are monotonic increasing functions of c and T. At low c and T, a small number of fiber seeds have sufficient time to grow in size, diffuse around and interact with one another via hydrodynamic effects before they are cross-linked with one another. This leads to the heterogeneous "bundle" network structure. As c and T increase, more fiber seeds emerge simultaneously and grow fast, which results in a more homogeneous network structure with short fibers. For a given set of c and T, we can effectively estimate the corresponding n and γ by comparing the experimental data with simulation results.

Our simulation works as follows: initially, n fiber seeds (short spherocylinders of aspect ratio 2) are placed in a periodic simulation box at random locations and orientations. We note that the initial aspect ratio of the fiber seed does not correspond to actual aspect ratio of a monomer, but rather makes it an anisotropic structural unit effectively representing a "fiber" in the early stage of the gelation. During each discretized time (MC) step, the following events occur:

- Each fiber grows in length via elongation at the two ends of the spherocylinder. The magnitude of the elongation δL_i is given by $\delta L_i = \epsilon L_i$, where L_i is the current length of the fiber and ϵ is a random number homogeneously distributed in $[0,\ \gamma]$.

- Each individual fiber has a translational and rotational motion, whose magnitudes are respectively denoted by $D_T^f(L_i)$ and $D_R^f(L_i)$ and are exponential functions of the fiber length L_i, i.e., $D_T^f(L_i) \sim \exp(-L_i/L_0)$ and $D_R^f(L_i) \sim \exp(-L_i/L_0)$. For fibers with length $L_i < L^*$, random translations and rotations are applied. For fibers with $L_i > L^*$, we consider that the fiber motions are biased such that two long fibers have the tendency to align with one another due to hydrodynamic effects. Specifically, the final orientation of the moved fiber is obtained by perturbing the orientation of the nearby "reference" long fiber.

- When two fibers are sufficiently close to one another, i.e., the distance d_f between the axis of spherocylinders is smaller than Δ, the fibers form a permanent cross-link with probability p_{cl}.

- A cluster of fibers can also have random translational and rotational motions, whose magnitudes D_T^c and D_R^c are generally much smaller than those of individual fibers.

The values of the simulated parameters, including the nucleation rate n and fiber growth rate γ, corresponding to various collagen concentrations and temperature values employed in experiments, will be discussed and provided in the following sections.

Simulated Collagen Growth Dynamics

To validate the kinetic MC method, we first employ it to simulate the growth dynamics of the collagen matrix with collagen concentration $c = 2$ mg/ml and maintained at $T = 23^o$C. The model parameters are determined such that the simulated growth dynamics reproduces the experimental observations described in previous sections. In particular, we denote the edge length of the cubic simulation box by ℓ_0 and use it as the unit for length. We have used $n = 300/\ell_0^3$ for the nucleation rate, $\gamma = 0.05$ for the growth rate, $D_T^f = 0.05\ell_0$ and $D_R^f = 0.15\pi$ for fiber translation and rotation, $D_T^c = 0.001\ell_0$ and $D_R^c = 0.05\pi$ for cluster translation and rotation. The critical distance for cross-linking is $\Delta = 0.005\ell_0$ with the cross-linking probability $p_{cl} = 0.5$. The critical fiber length beyond which fiber rotations are biased due to hydrodynamics effects is chosen to be $L^* = 0.25\ell_0$.

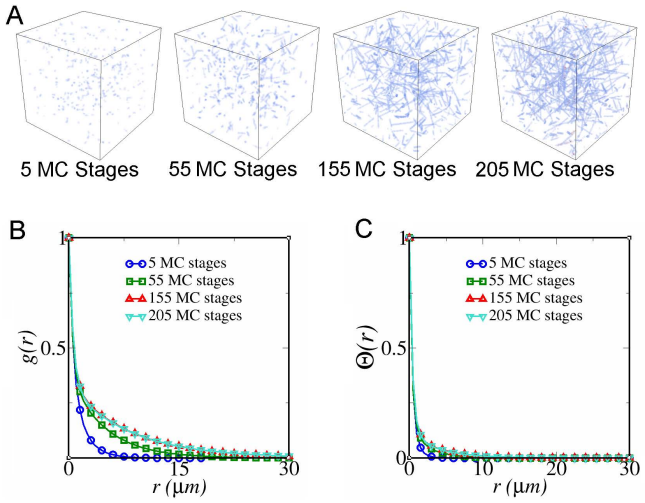

Fig. 4 The simulated growth dynamics of the collagen matrix at gelation temperature $T = 23^o$C. (A) Snapshots of simulated 3D collage network at different MC stages. (B) Two-point intensity correlation function associated with the simulated collagen matrix at different MC stages. (C) Nematic correlation function associated with the simulated collagen matrix at different MC stages.

Fig. 4A shows snapshots of a simulated growing collagen network in three dimensions at different MC steps after initialization. The specific MC steps selected are to match the corresponding snapshots of the experimental system shown in Fig. 1A. To make quantitative comparison with experimen-

tal data, we generate 2D gray scale images by convolving the 3D (binary) network with a point spread function represented as a Gaussian kernel. The width of the kernel is chosen to be $\sigma = 1.0$ μm, which produces reasonably smeared images that mimic the experimental data. The effects of different σ are systematically discussed in section S5 of Supporting Material. It is well established in heterogeneous material theory [44] that if a system is statistically homogeneous and isotropic, the two-point statistics computed from 2D slices of the material are representative of the full 3D structure. In section S6 of Supporting Material, we have verified for various simulated collagen networks that the intensity correlation functions obtained from 3D network and 2D slices are virtually identical. Thus, it is valid to compare the 3D simulation results and 2D experimental data. On the other hand, although the nematic correlation functions $\Theta(r)$ have different definitions in 2D and 3D systems, they both represent the degree of alignment between the fibers, and therefore will share the same trend as gelation temperature varies. Fig. 4B shows the two-point intensity correlation $g(r)$ at different gelation times (i.e., MC stages). The simulated density correlation functions can also be fitted very well with double exponential functions, i.e., $f(r) = a_1 \exp(-r/l_1) + a_2 \exp(-r/l_2)$. Similar to the experimental data, both l_1 and l_2 increase as gelation proceeds. The simulated nematic correlation function $\Theta(r)$ also possesses a growing length scale, which again is consistent with the experimental data. The agreement between the simulation and experimental results clearly demonstrates the validity and utility of kinetic Monte-Carlo growth model in modeling the collagen matrix.

Understanding the Effects of Gelation Temperature on Collagen Network

After validating the kinetic MC method with experiments, we now apply the simulations to better understand the observed temperature dependence of collagen matrix. In particular, we propose the following scenario to account for the experimental observations: At low gelation temperature T, the fiber nucleation rate is relatively low. Thus, a small number of fiber seeds (small nucleation rate) have sufficient time to grow in size, diffuse around and interact with one another before they are cross-linked with one another. At the point of cross-linking, the near-neighbor long fibers have developed a high level of orientational correlation (i.e., the tendency to be aligned with one another) due to hydrodynamic effects. This will lead to a heterogeneous network full of clusters of fibers. At high gelation temperature T, many fiber seeds emerge simultaneously (higher nucleation rate) and the growth rate is also higher. In this case, a percolating network quickly forms because cross-linking happens before significant orientational order can be achieved. This results in a homogeneous network structure with short fibers.

In order to verify the proposed scenario, we employ kinetic Monte-Carlo simulations and use least mean square fittings to search for the optimized set of n and γ at each temperature so that the density correlation function $g(r)$ of simulated network best matches the corresponding experimental data. This allows us to obtain the temperature dependence of the nucleation rate and growth rate, which we will elaborate on below.

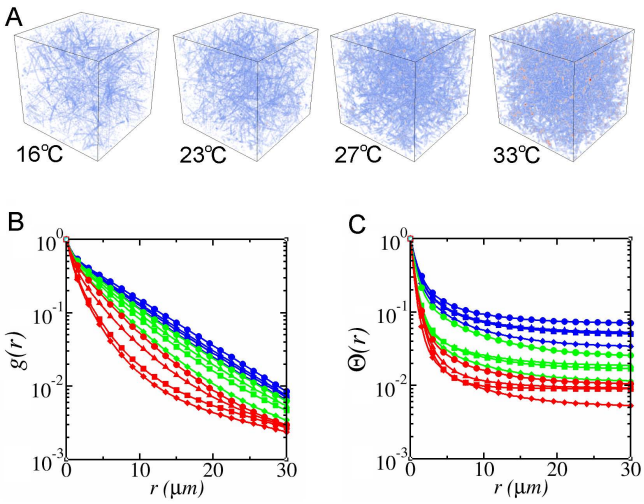

Fig. 5 Effects of temperature on the collagen network via simulation. (A) Snapshots of simulated 3D collagen networks formed at different gelation temperatures. (B) Two-point intensity correlation function corresponding to different collagen networks. (C) Nematic correlation function associated with different collagen networks. The color scheme and symbols for different temperature are the same as in Fig. 2. The simulated two-point statistics are quantitatively compared to their experimental counterparts by fitting the statics using double exponential functions, see section S7 of the Supporting Material.

Fig. 5A shows snapshots of the 3D collagen network corresponding to different temperatures. It can be clearly seen that as the gelation temperature increases, the network structure becomes more homogeneous, composed of shorter fibers with less orientational correlation. Also shown are the intensity correlation function $g(r)$ (Fig. 5B) and the nematic correlation $\Theta(r)$ function (Fig. 5C). The double-exponential fitting parameters (i.e., a_1, a_2, l_1 and l_2) and the global nematic order parameter $< s >$ as a function of temperature are provided in section S7 of Supporting Material. Similar to the experimental results, the length scales in g and Θ decrease as T increase, indicating a decrease of the degree of spatial and orientational correlation between the fibers in the network. In addition, for the intensity correlation function g, the weighting parameters a_1 increases with increasing T while a_2 decreases, indicat-

ing a decay of short-range correlation (e.g., that between bundles of fibers), which is consistent with experimental observations. Finally the simulated nematic order parameter $< s >$ decreases with temperature and almost vanishes at $T = 36^o$C, suggesting a continuous "phase transition" at the vicinity of this temperature. The good agreements between simulation and experimental results strongly support our proposed mechanisms for the temperature dependence of collagen network microstructures.

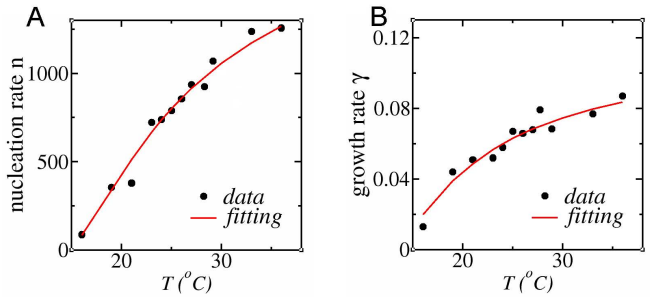

Fig. 6 Effects of temperature on the nucleation rate n (A) and growth rate γ as obtained from simulation (B). Both parameters exhibit an exponential dependence on the gelation temperature.

Our kinetic MC model also provides further insights on the temperature dependence of the parameters n and γ, which govern the gelation kinetics as well as the static microstructure. As shown in Fig. 6A, the nucleation rate exhibits an exponential dependence on the gelation temperature, i.e.,

$$n = A_1 \exp[-A_2/(T - A_3)], \tag{3}$$

where $A_1 = 2223\ell_0^{-3}$ is a scaling parameter and $A_2 = 11.6^o$C is an effective nucleation barrier, which could depend on the chemical composition and concentration of the collagen, and $A_3 = 13.2^o$C. This functional form is consistent with the prediction from classic nucleation theory[43]. Similarly, the growth rate also exhibits an exponential albeit weaker dependence on T, as shown in Fig. 6B, i.e.,

$$\gamma = B_1 \exp[-B_2/(T - B_3)], \tag{4}$$

where $B_1 = 0.12$, $B_2 = 8.93$ and $B_3 = 10.6$. This suggests that it is energetically favorable to elongate an existing fiber rather than creating a new one. As a result, the microstructure of collagen based ECM is more heterogeneous when formed at lower temperature.

We note that the temperature dependence of the nucleation rate and growth rate obtained here also qualitatively agree with previous work such as in[62]. For detailed discussion, see section S9 of Supporting Material.

CONCLUSIONS

In this article, we report the correlation-based microstructure characterization of collagen gel over a broad range of gelation temperatures. The two point correlation function $g(r)$ characterizes the spatial fluctuation of collagen fiber density, and can be further parameterized to obtain fiber thickness as well as fiber cluster sizes. We have demonstrated that as temperature increases, collagen fibers become shorter and form smaller clusters, resulting in a faster decay of the density correlations. The result is consistent with smaller pore sizes at higher temperature, which has also been observed for collagen gel formed at higher concentration[37,63].

In order to obtain the orientations of collagen fibers, we have developed a template-matching algorithm to calculate the coarse-grained nematic field directly from confocal reflection images. We have demonstrated that as temperature increases, the global nematic order decreases and $\Theta(r)$, the spatial correlation of nematic field also decays faster. This means that increasing temperature will lead to more randomly oriented fibers, and the local structure becomes more isotropic.

The correlation-based microstructure characterization presented here provides more detailed information than the global characterizations, such as pore size distribution[63]. However, neither the correlation functions, nor the pore size distribution uniquely determine the configuration of a collagen fiber network. Inspired by the close relation between growth dynamics and the equilibrium structures[9,41,64], we have developed a kinetic Monte-Carlo model based on the experiment measurements to simulate the growth dynamics of a collagen gel at specific gelation temperatures. Our model is validated by successfully reproducing the entire growth kinetics of collagen gel and suggests that the static structure of collagen gel is inherently connected with the growth kinetics. With our model, we showed that the nucleation rate, growth rate, and an effective hydrodynamic alignment of collagen fibers fully determines the spatiotemporal fluctuations of the density and orientational order of the collagen gel microstructure. Our model also enables us to determine the temperature dependence of the nucleation rate and growth rate, which are difficult to directly measure in experiments.

The structure of collagen gel determines the mechanical and transport properties of the fibrous ECM[6,7], both of which are key to collagen-based tissue engineering[4,65]. It is therefore of great interest to study the quantitative relations between microstructure characterization, the permeability, and rheology properties of collagen gel. The microstructures of collagen ECM in physiological settings are also closely related with the disease states of connective tissue. For instance, the shorter and less oriented fibers we observed at higher temperature resembles the collagen contracture in fibrosis[47]; longer and oriented collagen fibers have been recently shown to pro-

mote invasive transition of mammary acini[17]. These observations suggest an interesting future direction to apply our experimental characterization and simulation model to *in vivo* systems. In addition, our combined experimental and numerical study suggests that the gel microstructure can be tuned in a controllable fashion by varying a few environmental parameters. This would enable one to produce engineered gel structures for guided cellular behaviors.

MATERIALS AND METHODS

Preparing collagen gel

Gels were prepared from high-concentration rat tail collagen I in acetic acid (Corning, $\approx$ 10 mg/ml). The collagen was diluted with dH_2O, 10$\times$PBS (phosphate buffered saline), and 0.1 N NaOH to a final concentration of 2 mg/ml and a pH of 7.4. The temperature at which the collagen gel formed was regulated using a stage top incubator (ibidi Heating System, Universal Fit) equipped with an external temperature sensor (themo-couple type K). The temperature was set 30-60 minutes prior to the addition of collagen to allow the incubator to equilibrate. Preparation of the collagen solution was carried out on ice to prevent early gelation and two different methods were used to add the solution to the incubator.

The first method was used for experiments on the collagen growth dynamics in which imaging must begin immediately after the addition of collagen. Less than 60 seconds after neutralizing the collagen, the solution was injected through plastic tubing (Tygon S-54-HL, 0.04" ID) onto a glass bottom μ-dish (ibidi 35 mm) positioned above the microscope objective. Use of the plastic tube allows the collagen to be placed in the incubator without removing the lid and has a negligable effect on the thermal equilibrium of the system.

The second method was used for experiments on the temperature dependence of gel formation in which multiple gel samples were prepared at the same temperature from the same collagen solution. An 8 well μ-slide (ibidi) was placed in the incubator during equilibration with the external temperature sensor located in one of the wells. For gel formation below 23° C, the incubator was placed in a 4° C refrigerator, and for temperatures of 23° and above, the incubator was located on the lab bench at room temperature. After neutralizing the collagen solution, the lid of the incubator was removed and the remaining wells were filled with collagen. The time elapsed between neutralization and replacement of the incubator lid varied between samples but was always less than 3 minutes. After replacing the lid, all collagen samples were given at least one hour to fully gel before imaging. Removal of the lid and the addition of a larger total volume of collagen temporarily disrupts the thermal equilibrium of the system, so the temperature was monitored closely via the external sensor. Typical temperature versus time plots for these experiments are provided in the Supporting Material section S1.

Microscopy

Confocal reflection microscopy images of the collagen gels were taken using an inverted laser scanning confocal microscope (LSCM, Leica TCS SPE) with a 20$\times$ oil immersion objective. Samples were illuminated with a 532 nm laser and reflected light passed through a 30/70 RT filter and confocal pinhole before being collected by a photomultiplier tube detector (PMT). The scan size was 1024$\times$1024 pixels (367μm$\times$367μm) and reflected light intensity was collected as 8-bit gray scale images.

For imaging collagen growth dynamics, the microscope was equipped with an on stage incubator and the system was allowed at least 30 minutes for the temperature to equilibrate. Prior to the adding the collagen, the focal plane was set to the top surface of the glass μ-dish. The collagen was then injected into the incubator through a plastic tube such that the solution filled the area of the μ-dish directly above the objective. Immediately after addition of the collagen, the focal plane was moved approximately 50 μm into the sample and images were taken at one scan per second for 40-60 minutes. The time elapsed between collagen neutralization and the first scan was always less than 1 minute 30 seconds.

For multi-well collagen samples, one confocal z-stack was taken for each well with the first scan $\approx$10 μm above the glass to avoid reflection interference. 100 scans were taken per well with a 1.7 μm z-spacing between each scan.

Calculating nematic field by template-matching method

To calculate the nematic order of a test image, we have developed a template-matching method which includes three consecutive steps:

First, a series of template images with the same pixel resolution as the test image are generated. Each template image contains one line described by the equation $x\sin\theta - y\cos\theta = b$ where the origin of coordinate system is set at the center of the template image. For a pixel whose distance is d from the line $x\sin\theta - y\cos\theta = b$, the intensity is set to be $e^{-\frac{d^2}{\sigma^2}}$, where we choose $\sigma = 0.5$ pixel. For the 8 X 8 test images used in this study, we have generated 1800 templates $D_{b,\theta}(i,j)$ for $b \in [-2,2]$ (in steps of 0.5 pixel) and $\theta \in [0,180)$ (in step of 1 degree).

Next, we calculate the similarity score $R(b,\theta)$ between the test image $T(i,j)$ and the template images $D_{b,\theta}(i,j)$ as

$$R(b,\theta) = \frac{\sum_{i,j} T(i,j) * D_{b,\theta}(i,j)}{I(i,j) * D_{b,\theta}(i,j)} \quad (5)$$

here $I(i,j)$ is a matrix whose elements are all ones.

Finally, the nematic order $\mathbf{s}$ for the test image is calculated as

$$\mathbf{s} = \sum_{\theta} R(b,\theta)e^{2i\theta} \quad (6)$$

For a typical confocal image with pixel resolution 1024 X 1024, we divide it into 128 X 128 subregions, each containing a 8 X 8 test image. For subregions that only contain background, we define $\mathbf{s}(\mathbf{r}) = 0$. The size of the subregion is chosen to balance the accuracy of line detection and spatial resolution of the nematic field. We apply the template-matching method to each subregion and obtain the coarse-grained nematic field $\mathbf{s}(\mathbf{r})$.

Acknowledgments

Christopher Jones and Long Liang made equal contributions to this paper.

References

1 H. Lodish, A. Berk, S. L. Zipursky, P. Matsudaira, D. Baltimore and J. Darnell, *Molecular Cell Biology, 4th Edition, Chapter 22*, W. H. Freeman, 2000.
2 W. J. Matheson and M. Markham, *British Medical Journal*, 1952, 742–744.
3 T. Elsdale and J. Bard, *J. Cell Biol.*, 1972, **54**, 626–637.
4 R. A. Brown, *Exp. Cell Res.*, 2013, **319**, 2460–2469.
5 M. Djabourov, J. P. Lechaire and F. Gaill, *Biorheology*, 1993, **30**, 191–205.
6 S. B. Lindström, D. A. Vader, A. Kulachenko and D. A. Weitz, *Phys. Rev. E*, 2010, **82**, 051905.
7 Y. Jiao and S. Torquato, *Phys. Biol.*, 2012, **9**, 036009.
8 C. G. Bellow, A. H. Melcher and J. E. Aubin, *J. Cell Sci.*, 1981, **50**, 299–314.
9 G. Forgacs, S. A. Newman, B. Hinner, C. W. Maier and E. Sackmann, *Biophys. J.*, 2003, **84**, 1272–1280.
10 A. O. Brightman, B. P. Rajwa, J. E. Sturgis, M. E. McCallister, J. P. Robinson and S. L. Voytik-Harbin, *Biopolymers*, 2000, **54**, 222–234.
11 D. Vader, A. Kabla, D. Weitz and L. Mahadevan, *PLos ONE*, 2009, **4**, e5902.
12 Y. L. Yang and L. J. Kaufman, *Biophys. J.*, 2009, **96**, 1566–1585.
13 G. Cox, E. Kable, A. Jones, I. Fraser, F. Manconi and M. D. Gorrell, *J. Struc. Biol.*, 2003, **141**, 53–62.
14 R. M. Williams, W. R. Zipfel and W. W. Webb, *Biophys. J.*, 2005, **88**, 1377–1386.
15 K. R. Levental, H. Yu, L. Kass, J. N. Lakins, M. Egeblad, J. T. Erler, S. F. T. Fong, K. Csiszar, A. Giaccia, W. Weninger, M. Yamauchi, D. L. Gasser and V. M. Weaver, *Cell*, 2009, **139**, 891–906.
16 R. W. Tilghman, C. R. Cowan, J. D. Mih, Y. Koryakina, D. Gioeli, J. K. Slack-Davis, B. R. Blackman, D. J. Tschumperlin and J. T. Parsons, *PLos ONE*, 2010, **5**, e12905.
17 Q. Shi, R. P. Ghosh, H. Engelke, C. H. Rycroft, L. Cassereau, J. A. Sethian, V. M. Seaver and J. T. Liphardt, *Proc. Nat. Acad. Sci.*, 2014, **111**, 658–663.
18 E. Hadjipanyi, V. Mudera and R. A. Brown, *Cell Motil. Cytoskeleton*, 2009, **66**, 121–128.
19 S. Guido and R. T. Tranquillo, *J. Cell Sci.*, 1993, **105**, 317–331.
20 R. K. Jain, *Cancer Res.*, 1987, **47**, 3039–51.
21 A. G. Ogston, B. N. Preston and J. D. Wells, *Proc. R. Soc. London A*, 1973, **333**, 297–316.
22 L. Johansson, U. Skanzte and J. E. Löfroth, *Macromolecules*, 1991, **24**, 6019–23.
23 L. Johansson and J. E. Löfroth, *Colloid Interface Sci.*, 1991, **142**, 116–20.
24 L. Johansson, C. Elvingson and J. E. Löfroth, *Macromolecules*, 1991, **24**, 6024–9.
25 L. Johansson and J. E. Löfroth, *J. Phys. Chem.*, 1993, **98**, 7471–9.
26 H. A. Leddy, M. A. Haider and F. Guilak, *Biophys. J.*, 2006, **91**, 311–16.
27 A. E. et al., *Biopolymers*, 2008, **89**, 135–43.
28 T. Stylianopoulos, B. Diop-Frimpong, L. L. Munn and R. K. Jain, *Biophys. J.*, 2010, **99**, 3119–28.
29 A. P. Chatterjee, *J. Phys.: Condens. Matter*, 2011, **23**, 375103.
30 Y. Yang, L. M. Leone and L. J. Kaufman, *Biophys. J.*, 2009, **97**, 2051–60.
31 C. B. Raub, A. J. Putnama, B. J. Tromberg and S. C. George, *Acta Biomaterialia*, 2010, **6**, 4657–4665.
32 C. P. Broedersz, X. Mao, T. C. Lubensky and F. C. MacKintosh, *Nat. Phys.*, 2011, **7**, 983–8.
33 X. Ma, M. E. Schickel, M. D. Stevenson, A. L. Sarang-Sieminski, K. J. Gooch, S. N. Ghadiali and R. T. Hart, *Biophys. J.*, 2013, **104**, 1410–1418.
34 J. Feng, X. Mao and L. M. Sander, *arXiv:1402.2998*, 2014.
35 T. Lecuit, P. Lenne and E. Munro, *Annu. Rev. Cell Dev. Biol.*, 2011, **27**, 157–184.
36 F. J. O'Brien, B. A. Harley, M. A. Waller, I. V. Yannas, L. J. Gibson and P. J. Prendergast, *Tech. Health Care*, 2007, **15**, 3–17.
37 Y. L. Yang, S. Motte and L. J. Kaufman, *Biomaterials*, 2010, **31**, 5678–5688.
38 A. G. Ogston, *Trans. Faraday Soc.*, 1958, **54**, 1754–1757.
39 A. R. Takahashi, R. Kita, T. Shinozaki, K. Kubota and M. Kaibara, *Colloid Polym. Sci.*, 2003, **281**, 832–38.
40 W. Mickel and et al, *Biophys. J.*, 2008, **95**, 6072–6080.
41 J. Zhu and L. J. Kaufman, *Biophys. J.*, 2014, **106**, 1822–1831.
42 A. P. Chatterjee, *J. Phys.: Condens. Matter*, 2011, **23**, 155104.
43 P. M. Chaikin and T. C. Lubensky, *Principles of Condensed Matter Physics*, Cambrige University Press), 1995.
44 S. Torquato, *Random Heterogeneous Materials: Microstructure and Macroscopic Properties*, New York: Springer-Verlag), 2002.
45 M. Sahimi, *Heterogeneous Materials. Volume I: Linear Transport and Optical Properties*, Springer-Verlag), 2003.
46 M. Sahimi, *Heterogeneous Materials. Volume II: Nonlinear and Breakdown Properties, and Atomistic Modelling*, New York: Springer-Verlag), 2003.
47 J. J. Tomasek, G. Gabbiani, B. Hinz, C. Chaponnier and R. A. Brown, *Nat. Rev. Mol. Cell Biol.*, 2002, **3**, 349–363.
48 S. K. Boey, D. H. Boal and D. Discher, *Biophys. J.*, 1998, **75**, 1573–1583.
49 D. Discher, D. H. Boal and S. K. Boey, *Biophys. J.*, 1998, **75**, 1584–1597.
50 M. F. Coughlin and D. Stamenovic, *Biophys. J.*, 2003, **84**, 1328–1336.
51 A. E. Carlsson, *Biophys. J.*, 2006, **90**, 413–422.
52 A. Vaziri and A. Gopinath, *Nature Materials*, 2008, **7**, 15–23.
53 D. Shao, W. J. Rappel and H. Levine, *Phys. Rev. Lett.*, 2010, **105**, 108104.
54 M. Enculescu, M. Sabouri-Ghomi, G. Danuser and M. Falcke, *Biophys. J.*, 2010, **98**, 1571–1581.
55 M. Cirit and et al., *PLoS Comput. Biol.*, 2010, **6**, e1000688.
56 F. Ziebert, S. Swaminathan and I. S. Aranson, *J. R. Soc. Interface*, 2011, **9**, 1084–1092.
57 D. Gordon, A. Bernheim-Groswasser, C. Keasar and O. Farago, *Phys. Biol.*, 2012, **9**, 026005.
58 D. Shao, H. Levine and W. J. Rappel, *Proc. Natl. Acad. Sci. USA*, 2012, **109**, 6851–6856.
59 S. Wang and P. G. Wolynes, *Proc. Natl. Acad. Sci. USA*, 2012, **109**,

20820–20825.
60 H. Yamaoka, S. Matsushita, Y. Shimada and T. Adachi, *Biomech Model Mechanobiol*, 2012, **11**, 291–302.
61 U. Z. George, A. Stephanou and A. Madzvamuse, *J. Math. Biol.*, 2013, **66**, 547–593.
62 G. C. WooD, *Biochem. J.*, 1960, **75**, 598.
63 N. R. Lang, S. Münster, C. Metzner, P. Krauss, S. Schürmann, J. Lange, K. E. Aifantis, O. Friedrich and B. Fabry, *Biophys. J.*, 2013, **105**, 1967–1975.
64 R. M. Ziff and G. Stell, *J. Chem. Phys.*, 1980, **73**, 3492.
65 U. A. Stock and J. P. Vacanti, *Ann. Rev. Med.*, 2001, **52**, 443–451.